Supporting Information for

Evoking piezo-catalytic activity in $SrTiO_3$ perovskite via lattice strain

Zhenhua Cai[a], Zhiyong Liu[a*], Kun Guo[a], Bing Xie[a], Pengrong Ren[b], Haijun, Sun[a], Pu Mao[a], Zhiguo Wang[c], Longlong Shu[c]

[a]School of Power and Energy, Jiangxi Key Laboratory of Green General Aviation Power, Nanchang Hangkong University, Nanchang, 330063, China
[b]School of Materials Science and Engineering, Xi'an University of Technology, Xi'an, 710048, China
[c]School of Physics and Materials Science, Nanchang University, Nanchang, 330031, China
[*]Corresponding author, E-mail address: zyliumail@163.com

1 Experimental section

1.1 Characterization of catalysts

The crystal structure of samples was detected by X-ray diffractometer (XRD, D8ADVANCE, Brooke, Germany). Surface micromorphology, lattice striations, and energy spectra (EDS) were investigated using HR-TEM (Talos F200X, FEI, USA). Surface elemental states of the annealing STO samples were studied by X-ray photoelectron spectroscopy (XPS, Axis Ultra DLD, Shimadzu, Japan). Piezoelectric responses were characterized using force microscopy (PFM, MFP-3D-SA, Asylum Research). EPR spectra were measured at room temperature with a BRUKER EMX plus spectrometer. The diffuse reflectance and absorbance characteristics were examined by UV-Vis spectrophotometer (UV-9000, METASH, Shanghai, China). Fluorescence spectra were detected at the excitation wavelength of 425 nm using a fluorescence spectrophotometer (F97XP, Shanghai Cold Light Company, China) device.

1.2 Electrochemical measurements

The working electrode was fabricated by coating a powder sample on a conductive nickel foam substrate with a thickness of 0.5 mm. After several ultrasonic cleanings in deionized water and ethanol, the working electrode was constructed by depositing an appropriate amount of the sample on the nickel foam substrate. The prepared electrodes were cut into squares with an area of 10 mm × 10 mm after drying, and the transient piezoelectric current response and electrochemical impedance spectroscopy (EIS) were measured using a CHI760E electrochemical analyzer (Chenhua, Shanghai, China). The sample electrode, Ag/AgCl electrode, and platinum wire were used as working, reference, and counter electrodes, respectively. A 0.50 mol/L Na_2SO_4 solution was used as the electrolyte in all experiments.

1.3 Details of methylene blue (MB) degradation experiments

Preparation of 5 mg/L MB stock solution: weigh 0.005 g of MB standard sample accurately with an electronic analytical balance, add it into a beaker containing distilled water, stir continuously until it is completely dissolved, and then transfer it into a 1000 mL volumetric flask after natural cooling, and then volume it up to the scale line, and then place it in a room-temperature environment for storage and spare.

Experimental procedure: 10 mg of catalyst powder was dispersed in 10 mL of organic pollutant solution stirred under dark conditions for 60 min before vibro-catalyzing in order to achieve an adsorption-desorption equilibrium between the dye solution and the catalyst[1]. After that, a reaction vessel containing the mixed suspension was fixed in the center of an ultrasonic cleaner. During the catalytic process, circulating water was passed through the ultrasonic cleaner and a thermostatic water bath to maintain a stable water level and water temperature. To monitor the catalytic process in real time, 2 mL of the upper reaction solution was aspirated at regular intervals and centrifuged to separate the catalyst, and then the concentration of the solution was determined using a UV-vis spectrophotometer.

1.4 First principles calculation details

In this work, the calculation of the first-principles supercell model via CASTEP based on density functional theory (DFT)[2]. The PBE functional of general gradient approximation (GGA) by using the exchange correlation energy function of electron and electron interaction.

Considering the practicality and computational cost a 2×2×2 supercell of $SrTiO_3$ was performed and the optimized crystal structure was used to construct the (110) surface, which consists of 20 Sr atoms, 30 Ti atoms with 68 O atoms, and in order to prevent interactions between the periodic images, we used a vacuum of 20 Å in the z direction. During the structure optimization process, the atoms fixing the bottom 2 layers allowed the other layers to relax. The electron wave function is expanded by a set of plane waves with an energy cutoff of 571 eV. Surface calculations were performed using Monkhorst-Pack Brillouin sampling with k points of 1×1×1. The convergence criterion for the total energy is 1×10^{-4} eV/cell and for the atomic forces is 0.05 eV/Å. The adsorption energy Eads of the O_2 molecule is defined as:

$$E_{ads} = E_{surface+O_2} - E_{O_2} - E_{surface}$$

where $E_{surface+O_2}$, $E_{surface}$ and E_{O_2}represent the total energies of a O_2 on $SrTiO_3$(110) surface, a clean $SrTiO_3$(110) surface and a O_2 in gas phase, respectively.

1.5 Rietveld refinement details

In this work, Rietveld refinement of the coexistence of two phases in the annealed $SrTiO_3$ was performed using EXPGUI software. For the two-phase system, the

refinement and optimization of the phase ratio and other parameters were considered to determine the relative content of the two phases in the annealed $SrTiO_3$, and the parameters were adjusted so that the calculated and experimental spectra were consistent in terms of peak shapes, positions, and intensities. First, the experimental XRD data were imported into EXPGUI, which contains diffraction angle and intensity information and was the basis for refinement. CIF files of $SrTiO_3$ and $SrTiO_{2.6}$ were also imported, which provided the initial crystal structure information, the space group of Pm-3m ($a = b = c = 3.905$ Å, $\alpha = \beta = \gamma = 90°$) and P4/mmm ($a = b = 3.917$ Å, $c = 3.889$ Å, $\alpha = \beta = \gamma = 90°$) as well as the atomic positions, respectively. Next, an EXP file was generated in EXPGUI and the test parameters were entered, including the X-ray Cu Kα wavelength of 1.5406 Å, the scanning range of 20° - 80°, and the scanning step of 0.0167°. Then, according to the crystal properties of the samples and the shapes of the diffraction peaks, the pseudo-Urunner function was chosen to describe the diffraction peaks. Preliminary dual-phase structural models and parameters, including cell parameters and atomic coordinates, were established, and the corresponding information of the other phase was estimated at the same time.

In the refinement process, the background parameters were first fitted with a quadratic polynomial function $y = A + Bx + Cx^2$, adjusting A, B, and C to fit the background and adjusting the intensity scaling factor to match based on spectral comparisons. Subsequently, the structural parameters were refined. For the $SrTiO_3$ phase, the cell parameters (a, b, and c) and atomic coordinates were adjusted by the least squares method to match the experimental results and follow the symmetry of the two space groups. The fit between the calculated and experimental spectra was observed during the refinement process and evaluated on the basis of R factors (R_{wp}, R_p, etc.), with the expectation that R_{wp} was lower than 10%, and the quality of refinement and convergence were judged graphically.

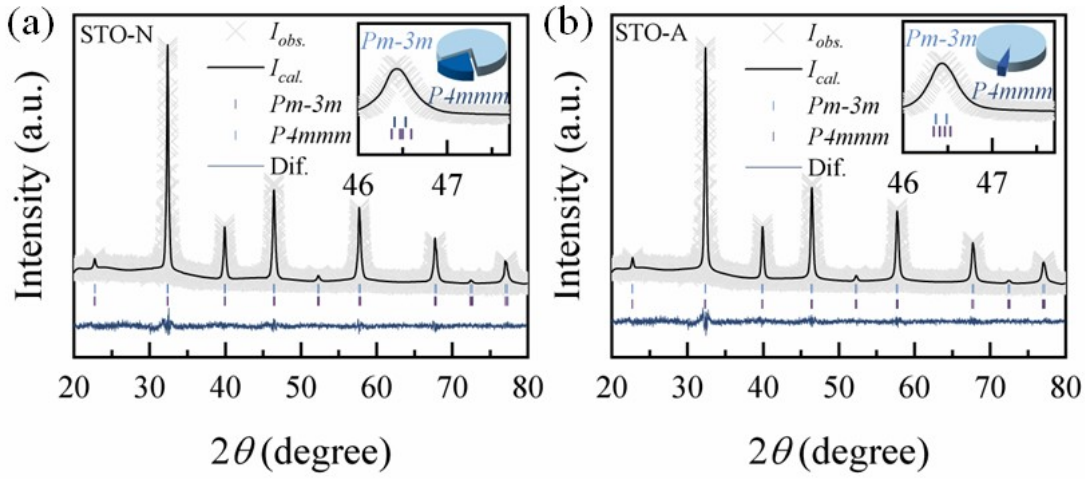

Fig. S1 Rietveld refinement of the (a) STO-N and (b) STO-A samples

Table S1 Rietveld refinement conditions and crystal structure parameters for the STO, STO-H, STO-N and STO-A samples.

Samples	STO	STO-H	STO-N	STO-A
χ^2	2.478	2.618	2.367	2.350
R_{wp} (%)	8.56	8.80	8.38	8.35
R_p (%)	6.76	6.77	6.51	6.41
Space group	Pm-3m	Pm-3m/P4mmm	Pm-3m/P4mmm	Pm-3m/P4mmm
Symmetry	C phase	C phase/T phase	C phase/T phase	C phase/T phase
a	3.912	3.911/3.915	3.911/3.914	3.912/3.914
b	3.912	3.911/3.915	3.911/3.914	3.912/3.914
c	3.912	3.911/3.903	3.911/3.906	3.912/3.908
V	59.875	59.879/59.883	59.844/59.851	59.857/59.843
Samples	STO	STO-H	STO-N	STO-A
χ^2	2.478	2.618	2.367	2.350
R_{wp} (%)	8.56	8.80	8.38	8.35
R_p (%)	6.76	6.77	6.51	6.41
Space group	Pm-3m	Pm-3m/P4mmm	Pm-3m/P4mmm	Pm-3m/P4mmm
Symmetry	C phase	C phase/T phase	C phase/T phase	C phase/T phase
a	3.912	3.911/3.915	3.911/3.914	3.912/3.914
b	3.912	3.911/3.915	3.911/3.914	3.912/3.914
c	3.912	3.911/3.903	3.911/3.906	3.912/3.908
V	59.875	59.879/59.883	59.844/59.851	59.857/59.843

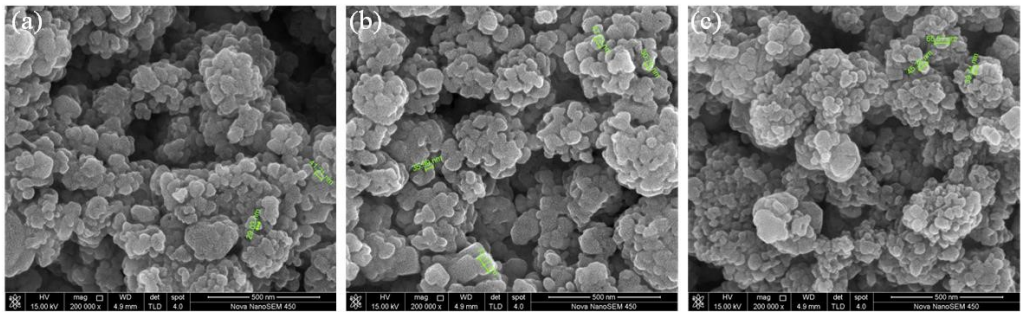

Fig. S2 SEM images and particle size distribution of (a) STO-H, (b) STO-N, and (c)STO-A samples.

Uniformly sized nanoparticles (~40 nm) are observed in the SEM morphology of the annealed STO samples. Also, by comparing Fig. S2a-c, the morphology and size of the heat-treated samples do not differ significantly and are all uniform nanoparticles. It indicates that the annealing treatments under different atmospheres do not affect the morphology of the STO samples.

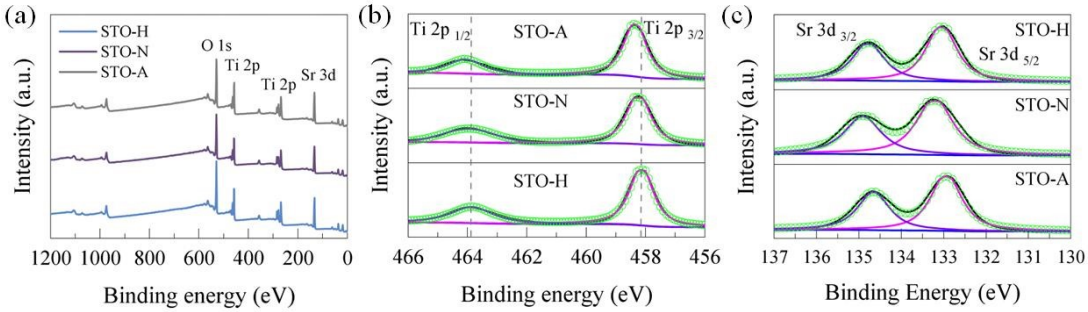

Fig. S3 (a)Wide-scan XPS spectra of STO-H, STO-N and STO-A samples. Corresponding narrow-scan XPS spectra for (b) Ti 2p, and (c) Sr 3d.

To verify the difference between the tetragonal phase $SrTiO_{2.6}$ and the cubic phase $SrTiO_3$ accommodating oxygen vacancies. The 2×2×2 supercells of $SrTiO_3$ and $SrTiO_{2.6}$ were modeled, respectively, to simulate the presence of oxygen vacancies by removing lattice oxygen inside the structure by the following equation:

$$E_f^v = E_{VO} + E_O - E_{perfect}$$

The formation energies were calculated, where E_{VO} and $E_{perfect}$ are the total energies of the crystal lattice systems with and without vacancies. E_O is the energy of a single oxygen atom. As can be seen from Table S2, the oxygen vacancy formation energy of $SrTiO_{2.6}$ is lower than that of $SrTiO_3$, proving that oxygen vacancy is easier to be formed in the tetragonal phase.

Table S2

Model	E_{vo}	$E_{perfect}$	E_o	E_f^v
$SrTiO_3$	-29945.42	-30351.46	-399.37	6.67
$SrTiO_{2.6}$	-29938.78	-30344.53	-399.37	6.38

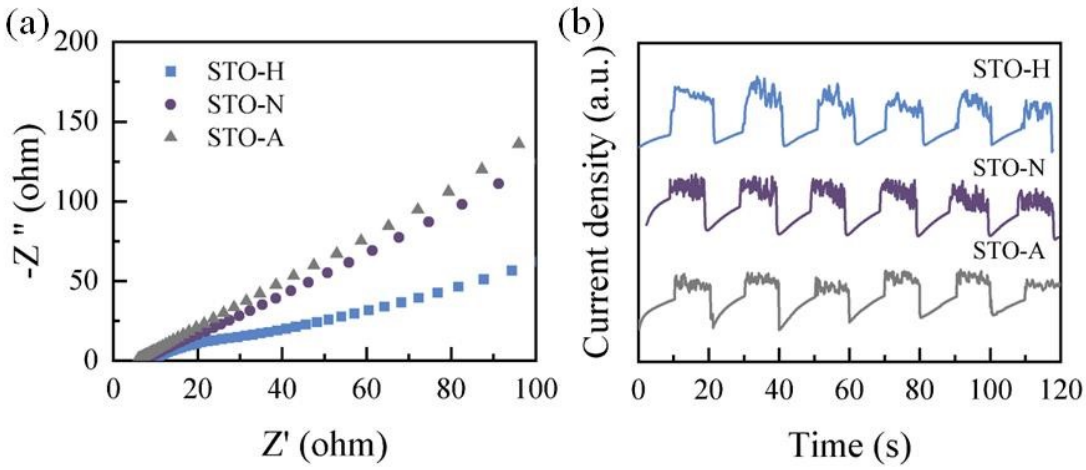

Fig. S4 (a) EIS Nyquist plots for different samples. (b) Transient current response in the dark for different samples.

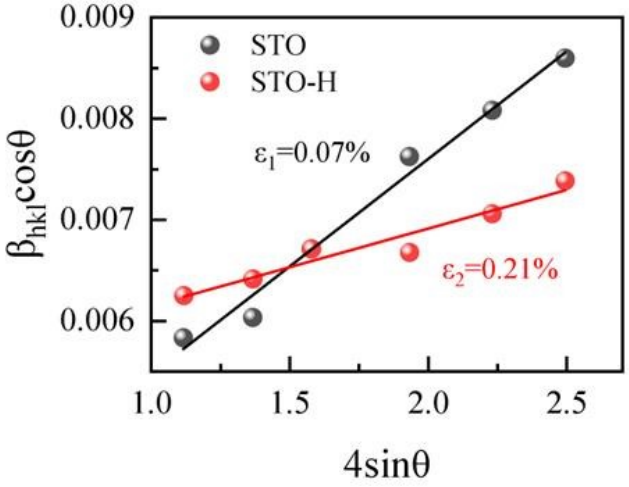

Fig. S5 Calculated lattice strains based on Williamson-Hall analysis.

The strain of the lattice was calculated by the Williamson-Hall method[3]：

$$\beta_T cos\theta = \varepsilon(4sin\theta) + \frac{K\lambda}{D}$$

β_T - the full width at half maximum of the XRD peak;

θ - the XRD peak position;

ε - the strain of lattice;

K - the shape factor;

λ - the wavelength of the X-ray source;

D - the crystallite size;

Based on the characteristic peak position and FWHM from XRD data, the Williamson-Hall curve, $\beta T cos\theta$ - $4sin\theta$ is plotted in Fig. S5. The strain of the unit cell is finally obtained by linearly fitting the curve and measuring the corresponding slope. The strains of STO and STO-H are 0.07% and 0.21%, respectively.

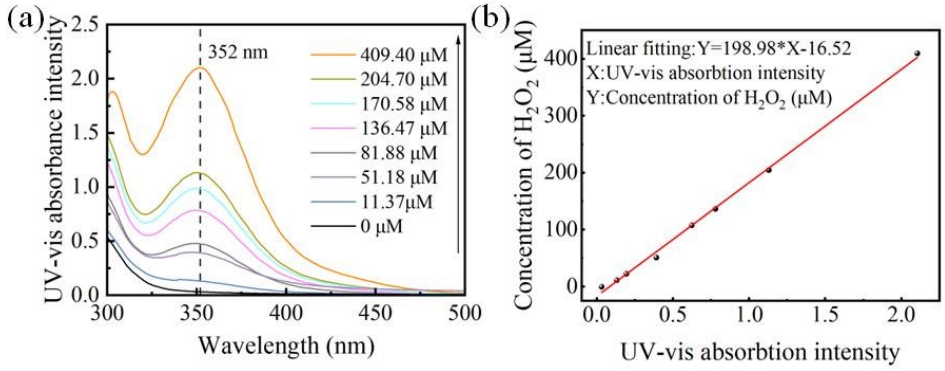

Fig. S6 (a) Calibration absorption spectrogram of H_2O_2 concentration. (b) Concentration and absorbance of H_2O_2 and fitted straight line.

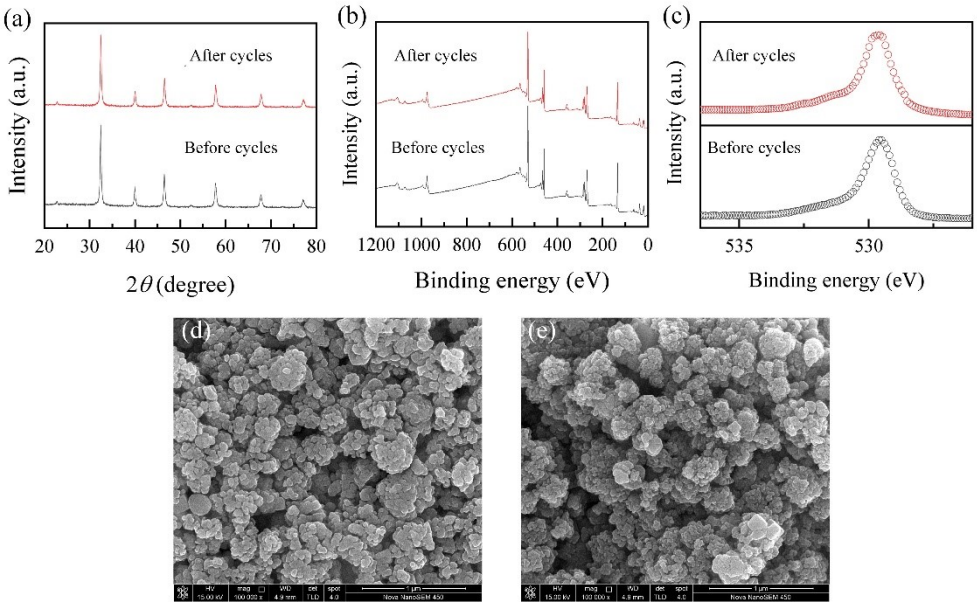

Fig. S7 (a) XRD patterns for STO-H before and after cyclic reaction. (b) Wide-scan XPS spectra of STO-H before and after cyclic reaction. (c) O 1s XPS spectra of the STO-H before and after cyclic reaction. SEM images of STO-H (d) before and (e) after cyclic reaction.

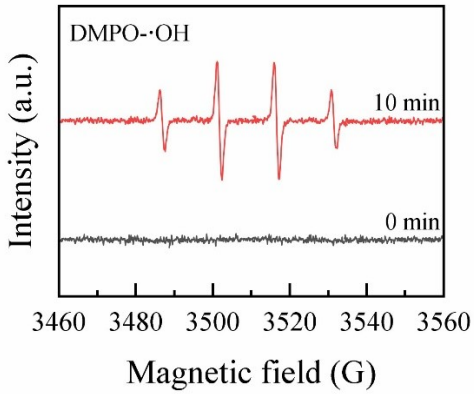

Fig. S8 EPR spectra of •OH active species.

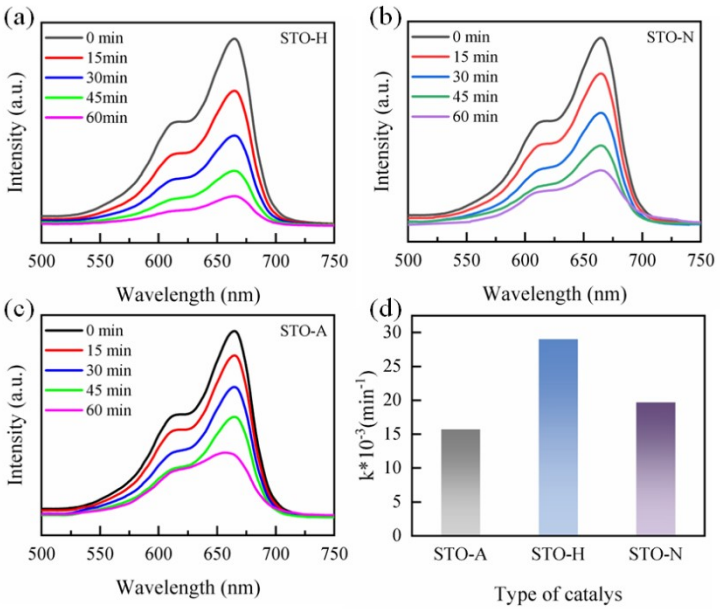

Fig. S9 Ultraviolet absorption spectra of degraded MB under ultrasonic vibration (a) STO-H, (b) STO-N, and (c) STO-A. (d) Piezo-catalyzed degradation rate.

References

1 M. R. Malekbala, M. A. Khan, S. Hosseini, L. C. Abdullah and T. S. Y. Choong, Adsorption/desorption of cationic dye on surfactant modified mesoporous carbon coated monolith: Equilibrium, kinetic and thermodynamic studies, J. Ind. Eng. Chem., 2015, **21**, 369-377,

2 H. Yue, K. Fang, Z. Gong, L. Chen, K. Guo, H. Liu, I. Tan, Z. Liu, B. Xie, J. Lu, Z. Chen, J. Tian and F. E. H. Tay, The mechanism of ferroelectric phase transformation in Gd_2O_3 modified BCZT ceramics: Experimental studies and first-principles calculations, Ceram. Int., 2024, **50**(7), 10416-10426.

3 B. Zhao, Z. Yan, Y. Du, L. Rao, G. Chen, Y. Wu, L. Yang, J. Zhang, L. Wu, D. W. Zhang and R. Che, High-entropy enhanced microwave attenuation in titanate perovskites, Adv. Mater., 2023, **35**(11), 2210243.